

## Quantitative multispectral biosensing and 1D imaging using quasi-3D plasmonic crystals

Matthew E. Stewart, Nathan H. Mack, Viktor Malyarchuk, Julio A. N. T. Soares, Tae-Woo Lee, Stephen K. Gray, Ralph G. Nuzzo, and John A. Rogers

*PNAS* published online Nov 3, 2006;  
doi:10.1073/pnas.0606216103

**This information is current as of November 2006.**

### Supplementary Material

Supplementary material can be found at:  
[www.pnas.org/cgi/content/full/0606216103/DC1](http://www.pnas.org/cgi/content/full/0606216103/DC1)

This article has been cited by other articles:  
[www.pnas.org#otherarticles](http://www.pnas.org#otherarticles)

### E-mail Alerts

Receive free email alerts when new articles cite this article - sign up in the box at the top right corner of the article or [click here](#).

### Rights & Permissions

To reproduce this article in part (figures, tables) or in entirety, see:  
[www.pnas.org/misc/rightperm.shtml](http://www.pnas.org/misc/rightperm.shtml)

### Reprints

To order reprints, see:  
[www.pnas.org/misc/reprints.shtml](http://www.pnas.org/misc/reprints.shtml)

Notes:

# Quantitative multispectral biosensing and 1D imaging using quasi-3D plasmonic crystals

Matthew E. Stewart<sup>\*†</sup>, Nathan H. Mack<sup>\*†</sup>, Viktor Malyarchuk<sup>†‡</sup>, Julio A. N. T. Soares<sup>†</sup>, Tae-Woo Lee<sup>§</sup>, Stephen K. Gray<sup>§</sup>, Ralph G. Nuzzo<sup>\*†‡¶</sup>, and John A. Rogers<sup>\*†‡¶</sup>

Departments of <sup>\*</sup>Chemistry and <sup>†</sup>Materials Science and Engineering, <sup>‡</sup>Frederick Seitz Materials Research Laboratory, University of Illinois at Urbana-Champaign, Urbana, IL 61801; and <sup>§</sup>Chemistry Division and Center for Nanoscale Materials, Argonne National Laboratory, Argonne, IL 60439

Edited by George M. Whitesides, Harvard University, Cambridge, MA, and approved September 21, 2006 (received for review July 21, 2006)

**We developed a class of quasi-3D plasmonic crystal that consists of multilayered, regular arrays of subwavelength metal nanostructures. The complex, highly sensitive structure of the optical transmission spectra of these crystals makes them especially well suited for sensing applications. Coupled with quantitative electrodynamic modeling of their optical response, they enable full multiwavelength spectroscopic detection of molecular binding events with sensitivities that correspond to small fractions of a monolayer. The high degree of spatial uniformity of the crystals, formed by a soft nanoimprint technique, provides the ability to image binding events over large areas with micrometer spatial resolution. These features, together with compact form factors, low-cost fabrication procedures, simple readout apparatus, and ability for direct integration into microfluidic networks and arrays, suggest promise for these devices in label-free bioanalytical detection systems.**

chemical sensing | nanoimprint lithography | surface plasmons | optical transmission spectra

**M**acromolecular biological interactions are critically important to the complex signaling and molecular recognition processes that occur in virology, cell signaling, DNA hybridization, immunology, DNA-protein interactions, and drug discovery, among others (1–5). Such systems can be probed by immobilizing one component of a binding pair on a surface and following the mass coverage change upon exposure to the complementary recognition element (6–9). Surface plasmon resonance (SPR) instruments that measure changes in refractive index near a metal surface accomplish this aim with high sensitivities, without the need for fluorescent labels (10, 11). Conventional SPR systems use prisms to couple light into a single surface plasmon mode on a flat, continuous metal (typically gold) film (12). This cumbersome experimental setup is difficult to integrate into low-cost, portable, image-based devices for rapid bioanalytical measurements of mass-limited samples (13). More recent work shows that metal nanostructured films and nanoparticles can be used for SPR type sensing without requiring coupling prisms using simple reflection or transmission configurations (14–19). However, these systems have some important limitations. First, even though some nanostructured films provide multiple plasmonic resonances, their current implementations involve metrics for binding sensitivities that are worse than those of conventional, single-resonance SPR devices (19–21). Second, fabrication of large area, spatially coherent arrays of highly uniform nanostructures (e.g., holes in films) that are best suited for sensing and imaging is cost prohibitive with conventional techniques (i.e., electron or ion beam lithography). Third, the basic nature of light interactions with these structures is complex, and many aspects remain uncertain (22–24), which has frustrated their optimized use for sensing. This work introduces a class of quasi-3D plasmonic crystals and an analysis approach that overcome these limitations. Quantitative computational electrodynamic modeling provides an understanding of the optics that can be exploited in a highly sensitive, full multispectral plasmonic approach to chemical sensing and 1D imaging. These capabilities are enabled in part by the

exceedingly high quality and unusual geometries of crystals formed, at low cost, with a type of soft nanoimprint lithography (25). Coupling these devices with microfluidic networks for quantitative spectroscopy and imaging of molecular binding events at the submonolayer level, with micrometer spatial resolution, demonstrates several of their attractive features.

## Results and Discussion

The crystals consist of large area square arrays of cylindrical wells (typically  $2.6 \times 10^6$  wells per sample) with diameters of  $\approx 480$  nm, depths of  $\approx 350$  nm, and center to center spacings of  $\approx 780$  nm, fabricated by soft nanoimprint lithography (25, 26) in films of a photocurable polyurethane. Uniformly depositing  $\approx 50$ -nm-thick gold films onto these samples coat the raised and recessed regions to create quasi-3D plasmonic crystals consisting of arrays of nanoscale holes in gold films with a second, physically separate level of isolated gold disks at the bottoms of the embossed wells (Fig. 1A). In normal incidence transmission mode, these devices exhibit strong spatial and wavelength-dependent intensity modulations involving absorptive, diffractive, and plasmonic effects (Fig. 1B).

Certain features in the transmission spectra of our crystals can be associated, at least partly, with local SPRs (LSPRs) on the rims of the nanoholes in the upper gold film, as well as in the lower metal disks. Important work by Dahlin *et al.* (27) has shown, in fact, how the LSPRs in random arrays of holes in gold films can be used for sensing. However, the spatially coherent, periodic nature of the holes and disks in our crystals create a much more varied and complex response that also includes Bloch wave surface plasmon polaritons (BW-SPPs) and Wood's anomalies. These types of responses do not appear in random 2D nanohole arrays (27, 28), nanoparticles (29, 30), or structures that do not exhibit high degrees of spatially coherent periodicity. BW-SPPs are standing waves corresponding to the coherent superposition of propagating SPPs. An approximate relation for the allowed wavelengths of a BW-SPP in our case is (22)

$$\lambda = \frac{P}{\sqrt{n_x^2 + n_y^2}} \sqrt{\frac{\epsilon_{Au}(\lambda)\epsilon_d}{\epsilon_{Au}(\lambda) + \epsilon_d}}, \quad [1]$$

Author contributions: S.K.G., R.G.N., and J.A.R. contributed equally to this work; M.E.S., N.H.M., J.A.N.T.S., T.-W.L., S.K.G., R.G.N., and J.A.R. designed research; M.E.S., N.H.M., V.M., J.A.N.T.S., T.-W.L., and S.K.G. performed research; N.H.M., T.-W.L., and S.K.G. contributed new reagents/analytic tools; M.E.S., N.H.M., V.M., T.-W.L., and S.K.G. analyzed data; and M.E.S., N.H.M., V.M., T.-W.L., S.K.G., R.G.N., and J.A.R. wrote the paper.

The authors declare no conflict of interest.

This article is a PNAS direct submission.

Freely available online through the PNAS open access option.

Abbreviations: SPR, surface plasmon resonance; LSPR, local SPR; BW-SPP, Bloch wave surface plasmon polariton; bBSA, biotinylated bovine serum albumin; PDMS, polydimethylsiloxane; RIU, refractive index unit.

<sup>¶</sup>To whom correspondence may be addressed. E-mail: r-nuzzo@uiuc.edu or jrogers@uiuc.edu.

© 2006 by The National Academy of Sciences of the USA

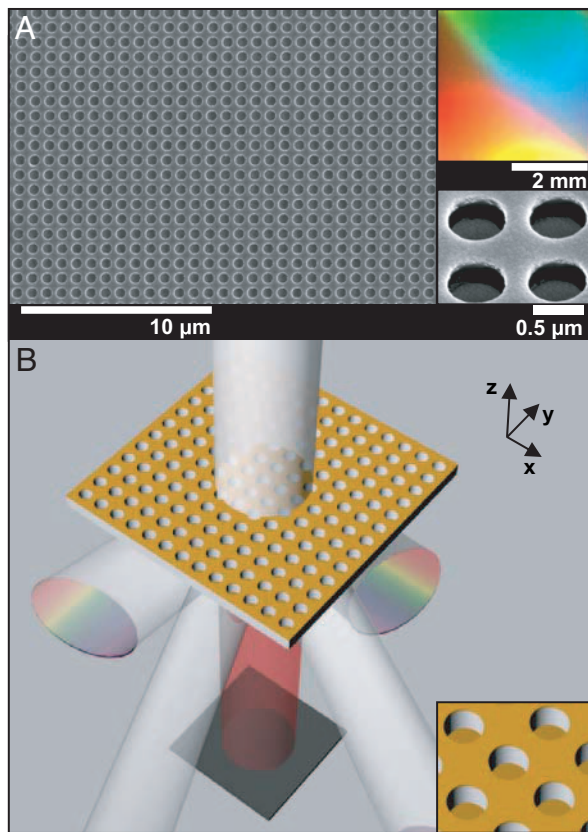


**Fig. 1.** Images and schematic illustrations of a quasi-3D plasmonic crystal. (A) Scanning electron micrograph (SEM) of a crystal. (Upper Inset) A low-resolution optical image illustrating the diffraction colors produced by these structures. (Lower Inset) A high magnification SEM that shows the upper and lower levels of gold. (B) Schematic illustration of the normal incidence, transmission mode geometry used to probe these devices. The intensity of the undiffracted, transmitted light is monitored across the UV, visible, and near-infrared regions of the spectrum. (Inset) A close-up schematic illustration of the crystal.

where  $P$  is the nanohole lattice spacing,  $\epsilon_{\text{Au}}(\lambda)$  is the wavelength-dependent relative dielectric constant for gold, and  $\epsilon_d$  is the relative dielectric constant of the material that interfaces with the gold. There are BW-SPPs associated with both the air/metal interfaces ( $\epsilon_d = 1$  for air) and the metal/polymer interfaces ( $\epsilon_d = 2.4336$  for polyurethane). The solutions of Eq. 1, for all possible integer values of  $n_x$  and  $n_y$ , excluding  $n_x = n_y = 0$ , yield the discrete zero-order wavelengths of the BW-SPPs. As shown in ref. 22, a Fano-like resonance profile consisting of a minimum, close to the position predicted by Eq. 1, and an adjacent maximum, can be associated with a given BW-SPP, which arises from interference between BW-SPPs and directly transmitted light. The other feature in our systems, the Wood's anomalies, involve diffracted light propagating parallel to the surface, similar to the BW-SPPs, but with a more spatially extended nature and without the direct involvement of plasmonic type responses. The Wood's anomalies satisfy an equation similar to Eq. 1, but with the argument of the second square root term being just  $\epsilon_d$ . The LSPRs, BW-SPPs, and Wood's anomalies can all overlap and couple with one another, leading to complex transmission spectra that are sensitive to the structural details and properties of the surrounding environment. The relative importance of the features and their couplings can be determined by rigorous electrodynamics calculations. These features provide additional information to enhance the sensing capabilities, especially in lithographically defined crystals, such as those

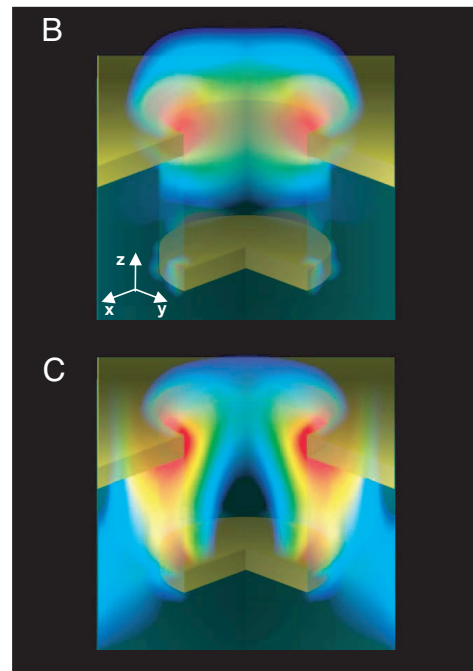
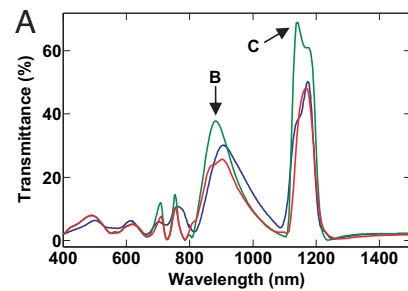


**Fig. 2.** Correlation of transmission spectral features with hole/disk plasmonic excitations. (A) Normal incidence transmission spectrum of a quasi-3D plasmonic crystal (blue), and rigorous electrodynamic modeling of the spectrum for an ideal crystal (green) and one that includes subtle isolated nanoscale grains of gold near the edges of the gold disks (red). (B) Computed electromagnetic field distribution associated with the resonance at 883 nm (labeled B in A). The intensity is concentrated at the edges of the nanoholes in the upper level of the crystal. (C) Field distribution associated with the resonance at 1,138 nm (labeled C in A), showing strong coupling between the upper and lower levels of the crystal.

described here, in which the geometry can be selected to optimize the nature and wavelength dependence of these features (Fig. 6, which is published as supporting information on the PNAS web site).

Full 3D finite-difference time-domain calculations with appropriate periodic boundary conditions (22, 31) were used to accurately model the transmission spectra and the electromagnetic field distributions in and around the metal nanostructures of the device (details of the calculations are given in *Supporting Text*, which is published as supporting information on the PNAS web site). Experimental and theoretical transmission spectra of a crystal with nanohole diameters of  $\approx 420$  nm, depths of  $\approx 350$  nm, and center to center spacings of  $\approx 720$  nm are shown in Fig. 2A. The two largest features in the spectra are labeled B and C. Peak B can be associated with LSPR behavior in the rims of the nanowells near the air/gold interface, as is shown in the calculated near-field intensity pattern (Fig. 2B). Indeed, we performed calculations for an isolated hole/disk structure and found just two transmittance peaks, one corresponding to direct

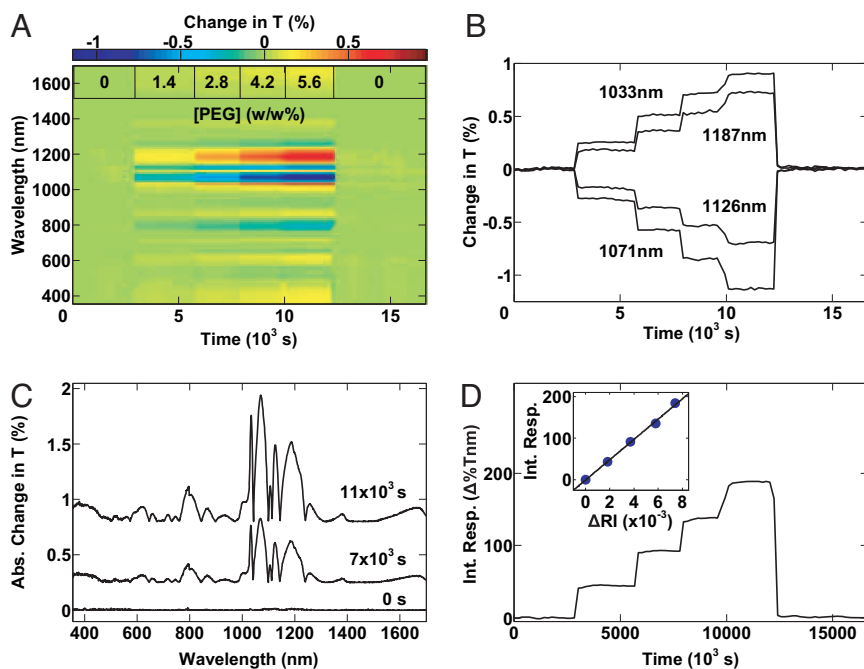


**Fig. 3.** Optical response of a plasmonic crystal to sequential injections of increasing concentrations of aqueous PEG solutions. (A) Color contour plot of the change in transmission ( $T$ ) as a function of wavelength and time (with the corresponding injection sequence overlaid on the plot). (B) Change in  $T$  as a function of time during the injection sequence, evaluated at several wavelengths. (C) Absolute value of the change in  $T$  as a function of wavelength, evaluated at different times. (D) Integrated multispectral plasmonic response as a function of time. (Inset) A linear correlation to the change in refractive index.

transmission through the thin film near 500 nm and another peak very close to the position of peak B corresponding to an isolated nanowell LSPR. In contrast, peak C involves overlapping Wood's anomaly and BW-SPP excitations on the gold disk/polymer side of the device that can be assigned, approximately, to  $n_x = \pm 1$ ,  $n_y = 0$  from Eq. 1 and the corresponding Wood's anomaly form. Thus, the near-field intensity associated with peak C is expected to be intense near the gold disk/polymer interface (Fig. 2C). Interestingly, the intensity also extends vertically up to the hole opening, indicative of strong coupling between disk and hole (Fig. 2C), a feature absent in random and ordered 2D nanohole arrays. Quantitative modeling of the experimental spectra required explicit consideration of the fine structural details in this region of strong coupling. In particular, it was necessary to introduce small (20–30 nm), isolated grains of gold along the sidewalls of the nanowells, just above the edges of the gold disks, to obtain good agreement between the experimental and theoretical spectra (Fig. 2A). The size of the grains and the extent to which they were deposited on the sidewalls of the relief structures was determined by high-resolution SEM (Fig. 7, which is published as supporting information on the PNAS web site). The pronounced sensitivity of the spectra to such subtle features highlights the demanding requirements placed on the fabrication procedures to realize structures with reproducible, sharp resonant features that can be modeled accurately. The soft nanoimprint technology used here, which can achieve replication fidelity down to the molecular regime (26, 32), is critical to the successful formation of the crystals. The plasmonic devices were found to be of high quality with few pixel defects ( $<10$ ) over large areas ( $\approx 20$  mm<sup>2</sup>), as determined by SEM (Hitachi S4700, 10 kV) imaging.

The transmission properties are also sensitive to the nature of the dielectric medium at the crystal surface (Fig. 8A, which is published as supporting information on the PNAS web site). The refractive index sensitivity of plasmonic sensors is often determined by measuring changes in the position or intensity

of a single resonance peak with the bulk refractive index of a surrounding fluid (19, 33). The bulk refractive index sensitivity of our quasi-3D plasmonic crystals was determined by passing solutions of increasing concentration of polyethylene glycol (PEG) (0–7.6 wt%) through a fluid flow cell containing a plasmonic crystal. Changes in peak positions and intensities were observed over most of the spectral range as the refractive index of the solution was increased. The most sensitive peak at  $\approx 1023$  nm was found to redshift and increase in intensity with progressively more concentrated aqueous solutions of PEG (Fig. 8B). Several crystals were measured, and this peak shifted linearly with a sensitivity of  $\approx 700$ – $800$  nm/RIU (RIU defined as refractive index unit; Fig. 8B Inset), and the intensity changed linearly with a sensitivity of  $\approx 2.5$ – $3.5$  Abs/RIU (Fig. 9, which is published as supporting information on the PNAS web site). These sensitivities exceed the responses reported for ordered 2D nanohole arrays ( $\approx 400$  nm/RIU) (20), random 2D nanoholes in gold (71–270 nm/RIU, 0.23–1 Abs/RIU) (19, 27, 34), nanoparticles and 2D nanoparticle arrays (76–200 nm/RIU, 0.46 Abs/RIU) (13, 29, 33), and silver films over nanowells (424–538 nm/RIU) (21). Surface binding events are typically monitored by following the response of such an individual peak or wavelength. However, this common method of analysis does not fully capture the sensitivity of our systems because it ignores information associated with the peak shifts and intensity changes occurring in the multiple plasmonic resonances in our spectra, created by the coherent couplings of the LSPRs, BW-SPPs, and Wood's anomaly responses exhibited by our systems. We propose a type of full, multispectral analysis that exploits this information to enhance the sensing capabilities and improve the signal-to-noise of our systems.

Multispectral analysis of a PEG calibration is shown in Fig. 3A, where a series of difference spectra, as referenced to the spectrum at time  $t = 0$ , illustrate changes in transmission (due to both peak position and intensity changes) throughout the wave-



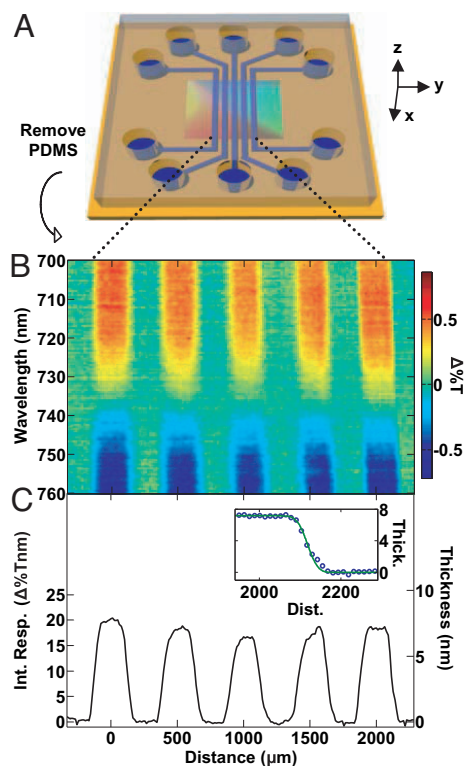


**Fig. 5.** Spatial imaging of fibrinogen nonspecifically adsorbed to the surface of a crystal. (A) A schematic illustrating the use of a multichannel PDMS microfluidic network to pattern the surface of a crystal (shown here with the multicolored appearance that characterizes these crystals). (B) Spectroscopic difference image of fibrinogen lines patterned on a crystal. (C) Spatially resolved integrated response and corresponding effective thickness illustrating binding events in the geometry of the microfluidic channels. (Inset) A measured step edge between a fibrinogen line and bare area of the crystal (blue symbols) and a fitted step edge with a Gaussian width of  $\approx 20 \mu\text{m}$ .

(Fig. 11, which is published as supporting information on the PNAS web site).

The capacities for quantitative biosensing, together with the high levels of spatial uniformity in the crystals, provide foundations for analytical imaging of large area multiplexed bioassays. As a simple demonstration, a plasmonic crystal patterned using a microfluidic device with five lines of nonspecifically adsorbed fibrinogen (Fig. 5A) was imaged in air using a white light source, monochromator, imaging optics, and a CCD array detector. Fig. 5B shows changes in transmission measured relative to an interchannel region on the crystal that did not come in contact with protein, such that the sample itself forms its own reference. The spectral image shows five stripes with the expected geometries, each corresponding to a region of the crystal patterned with fibrinogen. Converting the integrated response (Fig. 5C) to protein coverage using the PEG calibration data (Fig. 3) yields a spatial profile of the protein lines with a corresponding effective thickness of  $\approx 7 \text{ nm}$ , which is consistent with the molecular dimensions of fibrinogen (42, 43). Analysis of the step edges (Fig. 5C Inset) shows a characteristic width ( $20 \mu\text{m}$ ) that is only slightly larger than the resolution limit of the imaging optics ( $\approx 17 \mu\text{m}$ ). The  $\approx 3 \mu\text{m}$  of additional width in the plasmonic image can be associated with the propagation lengths of plasmons on these nanostructured crystals (44) and provides a lateral resolution comparable to current flat film SPR imaging systems (45–47). This micrometer-scale resolution, combined with the large area defect-free (and thus uniform response) aspects of the crystals, suggest a promising platform

for performing parallel diagnostic bioassays (see also Figs. 12–14, which are published as supporting information on the PNAS web site).

## Conclusions

This work demonstrates a form of highly sensitive quantitative chemical sensing that uses multispectral and spatially resolved techniques with quasi-3D plasmonic crystals. Theoretical modeling quantitatively accounts for the observed unique optical properties of these architectures and illustrates the complex electromagnetic field distributions around the multilevel nanostructured features in these systems. These devices can be fabricated at low cost and provide a platform for performing quantitative biochemical sensing and imaging with extremely high sensitivities in ways that facilitate miniaturization and integration into portable microfluidic lab-on-a-chip instrumentation.

## Materials and Methods

For additional details, see *Supporting Text*.

**Fabrication of Quasi-3D Plasmonic Crystals.** Polydimethylsiloxane (PDMS; Dow Corning, Midland, MI, Sylgard 184) and a photocurable polymer (PU; Norland Products, Cranbury, NJ, NOA 73) were used to fabricate nanostructured substrates via soft nanoimprint lithography as described (25). Briefly, casting and curing PDMS against a photolithographically defined pattern of photoresist on a silicon wafer formed PDMS molds with relief features in the geometry of square arrays of cylindrical posts. The PDMS molds were used to emboss NOA drop cast on a glass slide, which was then cured by UV light through the PDMS for 3 min. Removal of the mold yielded a layer of NOA with a relief structure identical to the pattern on the silicon master. A 50-nm-thick layer of gold was deposited on the NOA samples by electron beam evaporation (BOC Coating Technology, Fairfield, CA, Temescal, FC-1800).

**Transmission-Mode SPR Spectrophotometry.** Spectra of the plasmonic crystals were acquired on a Varian 5G UV-Vis-NIR spectrophotometer, operating in normal incidence transmission mode. A flow cell was constructed around the plasmonic crystals using a PDMS gasket sandwiched between a microscope slide and the sensor. Solutions were injected into the flow cell using a syringe pump (Harvard Apparatus) at a rate of 0.1 ml/min. Transmission spectra were continuously acquired as solutions were passed over the plasmonic crystal with a temporal resolution of  $\approx 90 \text{ s}$ .

**One-Dimensional Spectral Imaging.** A plasmonic crystal was patterned with five lines of nonspecifically adsorbed fibrinogen using a series of PDMS microfluidic channels ( $250 \mu\text{m}$  wide,  $500 \mu\text{m}$  pitch) and the channel outgas technique (48). After patterning, the PDMS device was removed and the crystal was rinsed with PBS and imaged using a home-built imaging system. A  $1 \times 5 \text{ mm}$  area of the crystal was illuminated with a white light source (Ocean Optics, Dunedin, FL, HL-2000) and imaged onto the slit of a monochromator (Acton Research, Acton, MA, SpectraPro 300i). The dispersed light exiting the monochromator was projected onto a liquid nitrogen cooled  $1024 \times 1024$  CCD (Princeton Instruments, Princeton, NJ) to generate a spectral image consisting of spatial information on one axis and spectral information on the other.

This work was supported by the U.S. Department of Energy, Division of Materials Sciences Award DEFG02-91ER45439, through the Frederick Seitz Materials Research Laboratory and Center for Microanalysis of Materials at the University of Illinois at Urbana–Champaign. The work at Argonne National Laboratory was supported by the Office of Basic Energy Sciences, Division of Chemical Sciences, Geosciences, and

1. Su X, Wu, YJ, Robelek R, Knoll W (2005) *Langmuir* 21:348–353.
2. Lin L, Harris JW, Thompson GR, Brody JP (2004) *Anal Chem* 76:6555–6559.
3. Rich RL, Myszkowski DG (2004) *Drug Discov Today* 1:301–308.
4. Shumaker-Parry JS, Aebersold R, Campbell CT (2004) *Anal Chem* 76:2071–2082.
5. Rao J, Yan L, Xu B, Whitesides GM (1999) *J Am Chem Soc* 121:2629–2630.
6. Whelan RJ, Zare RN (2002) *Anal Chem* 74:4570–4576.
7. Nelson KE, Gamble L, Jung LS, Boeckl MS, Naeemi E, Gollledge SL, Sasaki T, Castner DG, Campbell CT, Stayton PS (2001) *Langmuir* 17:2807–2816.
8. Xia N, Shumaker-Parry JS, Zareie MH, Campbell CT, Castner DG (2004) *Langmuir* 20:3710–3716.
9. Mrksich M, Grunwell JR, Whitesides GM (1995) *J Am Chem Soc* 117:12009–12010.
10. Whelan RJ, Zare RN (2003) *Anal Chem* 75:1542–1547.
11. Ostuni E, Chapman RG, Holmlin RE, Takayama S, Whitesides GM (2001) *Langmuir* 17:5605–5620.
12. Homola J (2003) *Anal Bioanal Chem* 377:528–539.
13. Nath N, Chilkoti A (2002) *Anal Chem* 74:504–509.
14. Barnes WL, Dereux A, Ebbesen TW (2003) *Nature* 424:824–830.
15. Xu Q, Bao J, Capasso F, Whitesides GM (2006) *Angew Chem Int Ed* 45:3631–3635.
16. Sun Y, Xia Y (2002) *Anal Chem* 74:5297–5305.
17. Sherry LJ, Chang S-H, Schatz GC, Van Duyne RP, Wiley BJ, Xia Y (2005) *Nano Lett* 5:2034–2038.
18. Yonzon CR, Jeoung E, Zou S, Schatz GC, Mrksich M, Van Duyne RP (2004) *J Am Chem Soc* 126:12669–12676.
19. Rindzevicius T, Alaverdyan Y, Dahlin A, Hook F, Sutherland DS, Kall M (2005) *Nano Lett* 5:2335–2339.
20. Brolo AG, Gordon R, Leathem B, Kavanagh KL (2004) *Langmuir* 20:4813–4815.
21. Hicks EM, Zhang X, Zou S, Lyandres O, Spears KG, Schatz GC, Van Duyne RP (2005) *J Phys Chem B* 109:22351–22358.
22. Chang S-H, Gray SK, Schatz GC (2005) *Opt Express* 13:3150–3165.
23. Murray WA, Astilean S, Barnes WL (2004) *Phys Rev B* 69:165407.
24. Lezec HJ, Thio T (2004) *Opt Express* 12:3629–3651.
25. Malyarchuk V, Hua F, Mack NH, Velasquez VT, White JO, Nuzzo RG, Rogers JA (2005) *Opt Express* 13:5669–5675.
26. Hua F, Sun Y, Gaur A, Meitl MA, Bilhaut L, Rotkina L, Wang J, Geil P, Shim M, Rogers JA (2004) *Nano Lett* 4:2467–2471.
27. Dahlin A, Zach M, Rindzevicius T, Kall M, Sutherland DS, Hook F (2005) *J Am Chem Soc* 127:5043–5048.
28. Prikulis J, Hanarp P, Olofsson L, Sutherland DS, Kall M (2004) *Nano Lett* 4:1003–1007.
29. Stuart DA, Haes AJ, Yonzon CR, Hicks EM, Van Duyne RP (2005) *IEEE Proc Nanobiotechnol* 152:13–22.
30. Haynes CL, McFarland AD, Zhao L, Van Duyne RP, Schatz GC, Gunnarsson L, Prikulis J, Kasemo B, Kall M (2003) *J Phys Chem B* 107:7337–7342.
31. Taflove A, Hagness SC (2005) *Computational Electrodynamics: The Finite-Difference Time-Domain* (Artech House, Boston).
32. Hua F, Gaur A, Sun Y, Word M, Niu J, Adesida I, Shim M, Shim A, Rogers JA (2006) *IEEE Trans Nanotechnol* 5:301–308.
33. McFarland AD, Van Duyne RP (2003) *Nano Lett* 3:1057–1062.
34. Dahlin AB, Tegenfeldt JO, Hook F (2006) *Anal Chem* 78:4416–4423.
35. Wilchek M, Bayer EA (1990) *Methods Enzymol* 184:5–13.
36. Huang TT, Sturgis J, Gomez R, Geng T, Bashir R, Bhunia AK, Robinson JP, Ladisch MR (2003) *Biotechnol Bioeng* 81:618–624.
37. Jung LS, Campbell CT, Chinowsky TM, Mar MN, Yee SS (1998) *Langmuir* 14:5636–5648.
38. Brewer SH, Glomm WR, Johnson MC, Knag MK, Franzen S (2005) *Langmuir* 21:9303–9307.
39. Haussling L, Ringsdorf H, Schmitt F-J, Knoll W (1991) *Langmuir* 7:1837–1840.
40. Hyun J, Ahn SJ, Lee WK, Chilkoti A, Zauscher S (2002) *Nano Lett* 2:1203–1207.
41. Kolomenskii AA, Gershon PD, Schuessler HA (1997) *Appl Opt* 36:6539–6547.
42. Snopok BA, Kostyukevych KV, Rengevych OV, Shirshov YM, Venger EF (1998) *Semicond Phys Quantum Elect Optoelect* 1:121–134.
43. Donahue JP, Patel H, Anderson WF, Wawiger J (1994) *Proc Natl Acad Sci USA* 91:12178–12182.
44. Kim DS, Hohng SC, Malyarchuk V, Yoon YC, Ahn YH, Yee KJ, Park JW, Kim J, Park QH, Lienau C (2003) *Phys Rev Lett* 91:143901.
45. Thiel AJ, Frutos AG, Jordan CE, Corn RM, Smith LM (1997) *Anal Chem* 69:4948–4956.
46. Brockman JM, Nelson BP, Corn RM (2000) *Annu Rev Phys Chem* 51:41–63.
47. Steiner G (2004) *Anal Bioanal Chem* 379:328–331.
48. Monahan J, Gewirth AA, Nuzzo RG (2001) *Anal Chem* 73:3193–3197.